



## Article

# Synthesis and Characterization of B<sub>4</sub>C-Based Multifunctional Nanoparticles for Boron Neutron Capture Therapy Applications

Maria Paola Demichelis <sup>1,2,\*</sup>, Agustina Mariana Portu <sup>3,4,5</sup> , Mario Alberto Gadan <sup>3</sup>, Agustina Vitali <sup>6</sup> ,  
Valentina Forlingieri <sup>6</sup>, Silva Bortolussi <sup>2,7</sup> , Ian Postuma <sup>7</sup> , Andrea Falqui <sup>8</sup> , Elena Vezzoli <sup>9</sup> ,  
Chiara Milanese <sup>1</sup> , Patrizia Sommi <sup>2,6</sup> and Umberto Anselmi-Tamburini <sup>1,2</sup>

- <sup>1</sup> Department of Chemistry, University of Pavia, V. le Taramelli 12, 27100 Pavia, Italy; chiara.milanese@unipv.it (C.M.); tau@unipv.it (U.A.-T.)
  - <sup>2</sup> Unit of Pavia, National Institute of Nuclear Physics, INFN, Via A. Bassi 6, 27100 Pavia, Italy; silva.bortolussi@unipv.it (S.B.); patrizia.sommi@unipv.it (P.S.)
  - <sup>3</sup> National Atomic Energy Commission (CNEA), San Martín C1429BNP, Argentina; agustina.portu@gmail.com (A.M.P.); mario.gadan@gmail.com (M.A.G.)
  - <sup>4</sup> National Scientific and Technological Research Council (CONICET), City of Buenos Aires C1425FQB, Argentina
  - <sup>5</sup> School of Science and Technology, National University of San Martín (UNSAM), San Martín B1650JKA, Argentina
  - <sup>6</sup> Department of Molecular Medicine, University of Pavia, Via Forlanini, 27100 Pavia, Italy; agostina.vitali@unipv.it (A.V.); valentina.forlingieri01@universitadipavia.it (V.F.)
  - <sup>7</sup> Department of Physics, University of Pavia, Via A. Bassi 6, 27100 Pavia, Italy; ian.postuma@pv.infn.it
  - <sup>8</sup> Department of Physics “Aldo Pontremoli”, University of Milan (Statale), Via Celoria 16, 20133 Milan, Italy; andrea.falqui@unimi.it
  - <sup>9</sup> ALEMBIC Advanced Light and Electron Microscopy BioImaging Center, San Raffaele Scientific Institute, DIBIT 1, Via Olgettina 58, 20132 Milan, Italy; vezzoli.elena@hsr.it
- \* Correspondence: mariapaola.demichelis01@universitadipavia.it; Tel.: +39-0382-987799



**Citation:** Demichelis, M.P.; Portu, A.M.; Gadan, M.A.; Vitali, A.; Forlingieri, V.; Bortolussi, S.; Postuma, I.; Falqui, A.; Vezzoli, E.; Milanese, C.; et al. Synthesis and Characterization of B<sub>4</sub>C-Based Multifunctional Nanoparticles for Boron Neutron Capture Therapy Applications. *Appl. Nano* **2024**, *5*, 33–47. <https://doi.org/10.3390/applnano5020004>

Received: 27 February 2024

Revised: 14 March 2024

Accepted: 19 March 2024

Published: 25 March 2024



**Copyright:** © 2024 by the authors. Licensee MDPI, Basel, Switzerland. This article is an open access article distributed under the terms and conditions of the Creative Commons Attribution (CC BY) license (<https://creativecommons.org/licenses/by/4.0/>).

**Abstract:** Nanoparticles composed of inorganic boron-containing compounds represent a promising candidate as <sup>10</sup>B carriers for BNCT. This study focuses on the synthesis, characterization, and assessment of the biological activity of composite nanomaterials based on boron carbide (B<sub>4</sub>C). Boron carbide is a compelling alternative to borated molecules due to its high volumetric B content, prolonged retention in biological systems, and low toxicity. These attributes lead to a substantial accumulation of B in tissues, eliminating the need for isotopically enriched compounds. In our approach, B<sub>4</sub>C nanoparticles were included in composite nanostructures with ultrasmall superparamagnetic nanoparticles (SPIONs), coated with poly (acrylic acid), and further functionalized with the fluorophore DiI. The successful internalization of these nanoparticles in HeLa cells was confirmed, and a significant uptake of <sup>10</sup>B was observed. Micro-distribution studies were conducted using intracellular neutron autoradiography, providing valuable insights into the spatial distribution of the nanoparticles within cells. These findings strongly indicate that the developed nanomaterials hold significant promise as effective carriers for <sup>10</sup>B in BNCT, showcasing their potential for advancing cancer treatment methodologies.

**Keywords:** nanomaterials; boron carbide; BNCT; neutron autoradiography

## 1. Introduction

Boron neutron capture therapy (BNCT) is an innovative binary radiotherapy for the treatment of aggressive and recurrent tumors. It is based on the neutron capture reaction taking place when the stable <sup>10</sup>B isotope is irradiated with low-energy (0.025 eV) thermal neutrons. Following the neutron capture, the unstable <sup>11</sup>B nucleus immediately decays, emitting high-LET (linear energy transfer) secondary particles: an α- particle (<sup>4</sup>He) and a Li nucleus. These particles deposit their energy in a short path length, between 4.5 μm and

10  $\mu\text{m}$ , which is comparable to the diameter of a single cell. These secondary particles can selectively kill tumor cells while sparing healthy neighboring tissues [1]. The effectiveness of BNCT is strongly dependent on two factors: the possibility of obtaining a high  $^{10}\text{B}$  concentration in the tumor and obtaining a sufficient thermal neutron flux in the target. It is generally accepted [2] that at least 20  $\mu\text{g}$  of  $^{10}\text{B}/\text{g}$  of tumor is needed to obtain an effective treatment, while the concentration of boron in the tumor must be at least three times the amount in the surrounding healthy tissues. The ideal  $^{10}\text{B}$  carrier should have prolonged retention times in the tumor and rapid clearance from the bloodstream [3–5]. Traditionally, BNCT relies on borated compounds such as boronophenylalanine (BPA) and disodium mercaptoundecahydro-*closo*-dodecaborate (BSH), which present a limited ability to deliver large amounts of boron to the tumor. Furthermore, these compounds are rapidly cleared from the tumor site and are easily degraded. Clinical trials based on the use of both BPA and BSH, independently or simultaneously, have been performed on recurrent glioblastoma multiforme, head and neck cancer, and recurrent lung, hepatic, or gastrointestinal cancers. Despite the positive outcome in some patients with tumor regression and few side effects, results are still variable [6–12]. Ongoing research aims to optimize boron delivery [13], through neutron beam characteristics [14–17] and treatment protocols, to maximize therapeutic outcomes and minimize potential side effects. The development of more selective  $^{10}\text{B}$  rich carriers is considered one of the greatest needs for BNCT. The use of B-rich nanomaterials represents a promising advancement for boron neutron capture therapy (BNCT) applications [18,19]. Several types of boron nanocarriers have been investigated. Liposomes, micelles, and dendrimers offer the advantage of encapsulating a high payload of boron compounds and facilitating their selective delivery to tumors. However, these nanostructures could manifest stability loss in physiological conditions, leading to the premature release of boron compounds before reaching the tumor site [2,20]. Conversely, nanoparticles of inorganic boron compounds present excellent stability under various physiological conditions. Moreover, nanoparticles of inorganic boron compounds offer the opportunity to achieve large and localized concentrations of  $^{10}\text{B}$  and present prolonged retention times within the organism [21,22]. Boron carbide ( $\text{B}_4\text{C}$ ) emerges as particularly noteworthy due to its high volumetric concentration of boron atoms, comparable to that of elemental boron. Furthermore, boron carbide exhibits exceptional chemical inertness and high biocompatibility [23,24].  $\text{B}_4\text{C}$  NPs have already been investigated as possible  $^{10}\text{B}$  carriers for BNCT [25–29]. The primary challenge associated with the use of  $\text{B}_4\text{C}$  NPs is related to their inherent hydrophobicity and low chemical reactivity, posing obstacles to achieving effective chemical functionalization. Furthermore, due to the low atomic weight of the component atoms,  $\text{B}_4\text{C}$  NPs are difficult to detect and quantify once they are incorporated by biological systems. To overcome these limitations, in this work, we present the synthesis of complex multifunctional composite nanomaterials obtained by combining  $\text{B}_4\text{C}$  as a  $^{10}\text{B}$  carrier with an MRI active moiety, represented by superparamagnetic iron oxide nanoparticles (SPIONs) and an optical fluorophore. This complex nanostructure will offer the possibility to not only exploit the BNCT therapeutic effect of a high-density boron carrier, but also to monitor its distribution in tissues and at the cellular level. These nanostructures (FeBNPs) are functionalized with the hydrophilic polymer poly(acrylic)acid (PAA), making them stable in aqueous suspension and biocompatible. MRI effectiveness is strongly dependent on the type of contrast agent [30–32]. The latter can influence either the longitudinal or transverse relaxation of protons, resulting in a positive (bright) contrast or a negative (dark) contrast, respectively. SPIONs have been extensively studied as negative contrast agents, as they usually present a large  $r_2/r_1$  ratio, which results in transverse relaxation enhancement. However, several studies have shown that ultrasmall SPIONs are excellent positive contrast agents as well. Some magnetite-based NPs have already been FDA-approved (Resovist, Feridex I.V, Gastromark), and their nontoxicity has long been accepted [33–36].

Synthesized FeBNPs were characterized for their size, morphology, and  $^{10}\text{B}$  content. Subsequent *in vitro* investigations were conducted to assess their interaction with the

HeLa cell line, examining their biocompatibility and extent of engagement with biological systems. The nanoparticles' potential as boron neutron capture therapy (BNCT) agents was evaluated through a combination of imaging techniques, including confocal and scanning electron microscopy, alongside intracellular neutron autoradiography. The quantitative measurement of  $^{10}\text{B}$  uptake was accomplished through inductively coupled plasma (ICP-OES) analysis.

## 2. Materials and Methods

In this work, we used  $\text{B}_4\text{C}$  nanopowder from Iolitec (IoLiTec-Ionic Liquids Technologies GmbH, Hilbronn, Germany, purity 99%), polyacrylic acid (PAA) (Mw~2000 Da, 50 wt%),  $\text{FeCl}_3 \cdot 6\text{H}_2\text{O}$  (purity 97%);  $\text{FeCl}_2 \cdot 4\text{H}_2\text{O}$  (purity > 99%)  $\text{NH}_4\text{OH}$  ( $\text{NH}_3$  28–30%), DiI (1,1'-dioctadecyl-3,3,3',3'-tetramethylindocarbocyanine perchlorate), 3-(4,5-dimethyl thiazolyl-2)-2,5-diphenyltetrazolium bromide, dimethyl sulfoxide from Sigma Aldrich; formaldehyde 16% from Cell Signaling, Hoechst 33342 from Sigma Aldrich, DE; and mowiol from Sigma Aldrich, DE.  $\text{dH}_2\text{O}$  was sterilized by filtration with 0.2  $\mu\text{m}$  pore size filter (Minisart, Sartorius AG, DE).

### 2.1. Synthesis of FeBNPs

The composite nanoparticles were obtained starting from the commercial  $\text{B}_4\text{C}$  NP powders. First, an aqueous suspension of  $\text{B}_4\text{C}$  NPs (with a concentration of 9 mg/mL) was obtained through treatment with an ultra-turrax at 6900 rpm for 1 h, through dispersion of 0.270 g of  $\text{B}_4\text{C}$  powders in 30 mL of sterile  $\text{dH}_2\text{O}$ . Then, 6 mL of  $\text{B}_4\text{C}$  NP suspension was added to an aqueous solution of 0.36 g of  $\text{FeCl}_3 \cdot 6\text{H}_2\text{O}$  (0.06 M) and 0.2 g of  $\text{FeCl}_2 \cdot 4\text{H}_2\text{O}$  (0.05 M). A total volume of 2 mL of  $\text{NH}_4\text{OH}$  (28–30%) was added to the suspension under vigorous stirring to obtain the precipitation of iron oxide nanoparticles. Subsequently, 5 mL of an aqueous solution of PAA 0.05 M was added to the mixture to make the produced NPs stable in water. The suspension was maintained at 30 °C for 1 h and then centrifuged at 100 kg for another hour. The supernatant was discarded, and the pellet, which represents the fraction of interest, was resuspended in sterile  $\text{dH}_2\text{O}$ . The suspension was then centrifuged at  $300 \times g$ . The pellet obtained at 300 g, which consists of the largest aggregates, was discarded, and the supernatant was separated and stored at RT. The produced nanoparticles suspension was stable for several weeks. To make FeBNPs detectable at the cellular level by optical and confocal microscopy, they were functionalized with the fluorophore DiI (FFeBNPs) using a modified solvent diffusion method proposed by Santra et al. [37]. A 1.2 mg/mL of DiI solution in DMSO was added drop by drop to 10 mL of FeBNPs under vigorous stirring. The stirring was maintained at RT for 1 h. During this time, the fluorophore intercalates in PAA's hydrophobic domains, adhering to the nanoparticle's surface. Subsequently, NPs were centrifuged at 100 kg for 1 h, the supernatant was discarded, and the pellet was resuspended in sterile  $\text{dH}_2\text{O}$ .

### 2.2. Nanoparticles' Characterization

X-ray diffraction (XRD) was carried out using a Bruker D2 diffractometer (Bruker Corp., Billerica, MA, USA) equipped with a copper X-ray source. We used a  $\theta - \theta'$  configuration, with a step size of  $0.03^\circ$  in  $2\theta$  and an acquisition time of 2 s for each step.

Micro-Fourier transform infrared spectroscopy ( $\mu$ -FTIR) was conducted using a  $\mu$ -FTIR Nicolet iN10 MX (Thermo Scientific, Waltham, MA, USA) equipped with a liquid nitrogen-chilled detector. Analysis was carried out in the ATR (attenuated total reflectance) mode within the range  $4000\text{--}500\text{ cm}^{-1}$  for a duration of 22 s. A volume of 10  $\mu\text{L}$  of suspension was air-dried on a microscopy glass, and three separate measurements were taken for each sample.

Dynamic light scattering (DLS) was performed using a Nano ZS90 DLS analyzer (Malvern Instruments, Malvern, UK). The suspension was diluted in water to obtain a concentration of about 1 mg/mL. Three measurements were acquired, each including 11 runs.

Scanning electron microscopy (SEM) and electron dispersive X-ray spectroscopy (EDS) were performed with a TESCAN Mira 3 XMY microscope (TESCAN ORSAY HOLDING s.a., Czech Republic) equipped with a field emission source and EDAX microprobe. Pictures were acquired using beam current voltage between 5 kV and 25 kV and either SE or BSE detectors. For the analysis, the NP suspension was first diluted, and 10  $\mu$ L of suspension was laid directly on a stub and air-dried in a closed container to avoid contamination. Samples are non-conductive. Hence, the samples were carbon-coated through vacuum evaporation (Cressington, Carbon Coater 208 carbon) prior to characterization.

Transmission electron microscopy (TEM) was conducted using a JEOL TEM. Samples were diluted 1:500 in  $dH_2O$ , and a drop (2  $\mu$ L) of suspension was placed on formvar/carbon-coated 250-mesh copper grids and left to dry for 10 min.

Thermo gravimetric analysis (TGA) was realized using a TGA Q5000 apparatus (TA Instruments, Wood Dale, DE, USA). The analysis was performed on 3–5 mg of NPs dried in an Abderhalden pistol at 50  $^{\circ}$ C for 1.5 h and subsequently placed on a Pt crucible and heated with a heating rate of 10  $^{\circ}$ C/min in air.

ICP-OES (inductively coupled plasma–optical emission spectroscopy) was carried out to quantify the amount of total boron both in the commercial boron carbide powders and in the suspension. Samples were first diluted in  $dH_2O$ , and then a certain amount of diluted sample was digested in a 1:1 =  $HNO_3:H_2SO_4$  mixture in 50 mL Teflon vessels. Digestions were carried out using *Mars Microwave* at 220  $^{\circ}$ C for 15 min at a pressure of 80 Bar. After digestion, the sample was allowed to cool to room temperature and 790 mg of mannitol was added to each sample to avoid the loss of volatile boron compounds. Specifically, for the analysis of commercial  $B_4C$  NPs, 10 mg of powder was added directly to 6 mL of the acidic mixture prior to digestion. Following digestion and mannitol addition, the samples were diluted 1:10 and analyzed via the method of standard addition. With regard to boron quantification of  $B_4C$  suspension and FeBNPs, 330  $\mu$ L of suspension was added to 6 mL of the acidic mixture and analyzed with the same procedure employed for  $B_4C$  powders. Each sample was digested and analyzed in triplicates through the method of standard additions.

### 2.3. Characterization of NPs–HeLa Cells Interaction

The HeLa cell line derived from uterine adenocarcinoma and used for these experiments was generously provided by T.L. Cover, Vanderbilt University, Nashville, TN, USA. Cells were cultured in T10 flasks and maintained in incubation at 37  $^{\circ}$ C in 5%  $CO_2$  atmosphere. The culture medium was composed of DMEM medium (4.5 g/L glucose, Euroclone, IT, Pero, Italy), supplemented with FBS (10%) and L-glutamine 2 mM. Evaluation of FeBNPs toxicity was conducted using MTT (3-(4,5-dimethyl thiazolyl-2)-2,5-diphenyltetrazolium bromide) assay [38]. Cells were seeded in 6-well plates (Greiner Bio-One International GmbH, Monroe, NC, USA). After 24 h, when cells reached 80% confluency, they were exposed to FeBNPs suspensions diluted 1:10, 1:30, 1:50, 1:100, and 1:200 in medium for 2 h. The dilutions correspond to 44.5, 22.25, 11.12, 5.56, and 2.78  $\mu$ g of  $^{10}B$ , respectively. Following incubation, the medium was removed, and HeLa cells were washed with PBS before incubating in fresh medium without nanoparticles for an additional 2 h at 37  $^{\circ}$ C. Subsequently, MTT solution (0.5 mg/mL) was added, and after 1 h and 30 min of incubation, the medium was discarded, and DMSO was introduced in fresh medium to dissolve the formazan crystal. Absorbance at 570 nm was measured using a plate reader.

For confocal microscopy analysis, HeLa cells were seeded on 18  $\times$  18 mm glass coverslips in 35 mm Petri dishes. Cells were used at approximately 60% of confluence for incubation with varying concentrations of fluorescent FeBNPs. After the treatment, cells were fixed with formaldehyde 4% in PBS for 15 min at room temperature, and the nuclei were stained with Hoechst333342. Finally, the coverslip was mounted upside down on a microscope glass slide (Manzel Glaser), using a drop of mowiol. Confocal microscopy was performed using the Leica TCS SP5 II confocal microscope, equipped with PL APO 40 $\times$ /1.25 NA or 63 $\times$ /1.40 NA objectives and a motorized stage.

For SEM characterization, HeLa cells were seeded in a 35 mm Petri dish and incubated with FeBNPs when at 30% confluence. After the incubation with FeBNPs, the medium was discarded, and cells were washed with PBS and subsequently fixed with glutaraldehyde (2.5% in cacodylate buffer 0.1 M pH 7.3) at room temperature for 2 h. For the analysis, Petri dishes were attached to the stub through conductive graphite tape, and the samples were carbon-coated through high vacuum evaporation.

For TEM imaging, HeLa cells were treated with FeBNPs for 30 min and 2 h. Subsequently, cells were fixed in 2% glutaraldehyde in cacodylate buffer 0.1 M pH 7.3 for 20 min at room temperature, then centrifuged for 1 min at 13,000 rpm. The cell pellets were further fixed for 24 h at 4 °C and post-fixed for 1 h in a 2% osmium tetroxide water solution. After several washings in bi-distilled water, the pellets were placed in 1% uranyl acetate water solution and left for 1 h at room temperature. Samples were dehydrated by a graded ethanol series (70%, 80%, 90%, 100%, and acetone for 10 min each) and finally embedded in Epon resin. After curing at 60 °C for 48 h, thin sections were obtained by cutting the embedded samples using an UltraCut E Ultramicrotome (Reichert) and placed on 300-meshes copper grids, which were then observed using a Talos L120C G2 transmission electron microscope (Thermo Fisher Scientific Inc. Waltham, MA, USA) working at an acceleration voltage of 120 kV, equipped with a lanthanum hexaboride thermionic source and a bottom-mount Ceta Thermofischer 4 k × 4 k CMOS camera.

For cytofluorimetric analysis, HeLa cells were seeded in culture flask at  $6.0 \times 10^4$  cells/cm<sup>2</sup>m, and after 24 h, treated with or without NPs. The cells were detached using trypsin–EDTA and fixed in 10% formalin to be processed for flow cytometry. We used a BD FACSLyric flow cytometer equipped with violet (405 nm, 40 mW), blue (488 nm, 20 mW), and red (640 nm, 40 mW) lasers (BD Biosciences, Franklin Lakes, NJ, USA). For each sample, at least  $5.0 \times 10^5$  events were acquired at a flow rate of 200 µL/mL. Emission from the NPs was stimulated with the blue laser, and the fluorescence was detected using the band-pass filter (FACSLyric, 586/42 nm). Experiments were carried out in three replicates.

The boron uptake from HeLa cells was quantified using ICP-OES analysis. HeLa cells were seeded in T25 flasks. When a concentration of about  $10^6$  cells/mL was reached, FeBNPs were added directly to the medium. Incubation took place for 30 min and 2 h. Following incubation, the medium was discarded, and cells were washed with PBS. After washing, the cells were detached from the substrate with trypsin, resuspended in DMEM medium, and centrifuged at  $160 \times g$  for 5 min. The pellet was washed in PBS, centrifuged again, and resuspended in 1 mL PBS. The obtained samples were then digested in a 1:1 = HNO<sub>3</sub>:H<sub>2</sub>SO<sub>4</sub> mixture in 50 mL Teflon vessels. Specifically, cells were added to 6 mL of acid mixture. Digestions were carried out using Mars Microwave at 220 °C for 15 min at a pressure of 80 Bar. After digestion, the sample was allowed to cool to RT, and 790 mg of mannitol was added to each sample to avoid the loss of volatile boron compounds [39,40]. Samples were diluted, and the method of standard additions was carried out.

To perform intracellular neutron autoradiography and to carry out <sup>10</sup>B micro-distribution studies, HeLa cells incubated with FeBNPs were grown on solid-state nuclear tracks detectors (SSNTDs) that later underwent irradiation. This technique is based on previous works by Portu et al. [41–43]. Specifically, the SSNTD (Lexan, made of polycarbonate of 250 µm thickness) was cut into round dishes 30 mm in diameter. After transferring the Lexan into 35 × 35 mm Petri dishes, HeLa cells ( $1.5 \times 10^5$  cells/mL) were seeded and subsequently incubated with varying FeBNP concentrations for 30 min, 2 h, and 6 h. Following incubation, the cells were washed twice with PBS and fixed with 2.5% glutaraldehyde. Samples were irradiated at  $10^{12}$  or  $10^{13}$  n/cm<sup>2</sup>s neutron fluences at the RA-3 reactor (Ezeiza Atomic Centre, CNEA, Buenos Aires, Argentina). Once the samples were irradiated, both the cell imprints and nuclear tracks were developed. To create the cell imprints, the fixed cells on the SSNTD underwent staining with hematoxylin for 15 min initially. Subsequently, they were subjected to UV-C irradiation for 5 min, using a 15 watt, 254 nm wavelength TUV G15T8 (Philips, Holland) lamp. The irradiance at the irradiation position was determined to be 5.7 mW/cm<sup>2</sup> through measurements with

a radiometer (International Light Technologies ILT77). Following UV-C exposure, the samples were cleaned from organic material using trypsin and underwent etching with PEW solution (consisting of 30 g KOH + 80 g ethyl alcohol + 90 g distilled water) for 4 min at 70 °C. This treatment induced the enlargement of latent tracks, rendering them visible through optical microscopy. Pictures were acquired with an optical microscope (Olympus BX51), coupled to a CCD camera (Olympus DP70). Light conditions were adjusted to achieve consistently reproducible images.

### 3. Results

#### 3.1. $B_4C$ NPs' Characterization

SEM analysis of the commercial boron carbide nanopowders evidenced a high degree of aggregation (Figure 1A). The treatments with ultra-turrax significantly decreased the degree of aggregation and allowed us to obtain a stable aqueous suspension (Figure 1B). The effectiveness of the treatment with the ultra-turrax could not be verified through DLS, as boron carbide powders are strongly hydrophobic and the measurements could not be obtained prior to functionalization. TEM characterization of the obtained aqueous suspension showed irregularly shaped, polydispersed nanoparticles aggregates with sizes ranging from 10 to 60 nm (Figure 1C). The XRD patterns confirmed the presence of the rhombohedral structure of  $B_4C$  NPs (space group R-3m), but highlighted the presence of impurities, namely graphite and  $H_3BO_3$  (Figure 1D). Graphite and boric acid impurities probably derive from the synthesis procedure [44–47]. Rietveld analysis was not performed owing to the presence of a poorly crystalline graphite impurity, which could prevent a reliable quantitative analysis. Additionally, the shoulder at 20 degrees, overlapping with the graphite peak, may be attributed to the presence of amorphous boron carbide. Consequently, total boron content was quantified through ICP regardless of the phase. The presence of these impurities was also detected through  $\mu$ -FTIR (Figure 1E). The boron content was quantified through ICP both in the starting  $B_4C$  powders and in the suspension used to carry out the synthesis of composite FeBNPs. From ICP-OES analysis, the boron content in the starting powders was found to be a third of the expected value, because of the presence of impurities. A similar result was obtained for the water suspension obtained through the ultra-turrax. Pristine nanopowders digested as reported in Section 2.2 resulted in 32.3% of the theoretical content of  $B_4C$  (calculated by weight over volume). In the aqueous suspension, the ICP analysis revealed 31.5% of the theoretical  $B_4C$  amount.

Thermogravimetric analysis carried out in air (TGA curve in Figure 1F) confirmed the presence of significant amounts of impurities in the  $B_4C$  nanopowders: the first weight loss (25–400 °C) is composed of several steps attributable to the dehydration of the sample (25–100 °C) and to the decomposition of boric acid to metaboric acid (100–145 °C), pyroboric acid (145–160 °C), and boron oxide (160–360 °C), respectively [48]. At 600 °C, the TGA curve shows a weight increment due to the oxidation of the sample to  $B_2O_3$ , followed by a weight loss above 700 °C, corresponding to the loss of volatile species ( $CO$ ,  $CO_2$ ) due to the oxidation of graphite [48,49].

#### 3.2. FeBNPs' Characterization

FeBNPs' water suspension is stable for weeks. The NPs present a mean hydrodynamic diameter of  $55 \pm 13$  nm. Successful coating with poly(acrylic acid) was confirmed by zeta potential measurements that showed a negatively charged surface ( $-36 \pm 0.9$  mV). The presence of PAA was also detected through  $\mu$ -FTIR. The same characterization confirmed the presence of iron oxide NPs (Figure 2B,C). The phase composition of FeBNPs was evaluated through XRD. Figure 2C shows the presence of a spinel structure that can be attributed to magnetite, with a lattice constant of 8.37 Å. The lattice parameter lies between that of maghemite (8.3515 Å) and magnetite (8.396 Å). This is due to the partial oxidation of  $Fe^{2+}$  to  $Fe^{3+}$  that occurs when samples are synthesized in or exposed to air. No peaks of the boron carbide phase can be observed, probably because of the shielding from the iron oxide NPs, which are heavier and with a higher concentration than  $B_4C$ . The average crystallite

size was calculated using the Debye Scherrer equation applied on (220), (311), and (400) peaks, and was found to be 3.7(0.4) nm. This crystallite size agrees with the TEM images, which show spherical, ultrasmall iron oxide NPs with diameters ranging from 4 nm to 6 nm, with an outer layer probably constituting the poorly crystalline region [28]. TEM also confirmed the successful co-localization of SPIONs and  $B_4C$  NPs, as the latter seem to be surrounded by the ultrasmall SPION, and no bare  $B_4C$  NPs are observed in the sample (Figure 2B). However, both SEM and TEM highlighted that SPION distribution around  $B_4C$  NPs is irregular. In fact, comparing SEM images of the same area obtained using different detectors (SE, BSE), it is possible to notice the non-homogeneous distribution of the heavier SPIONs around the  $B_4C$  nanoparticle (Figure 2A).

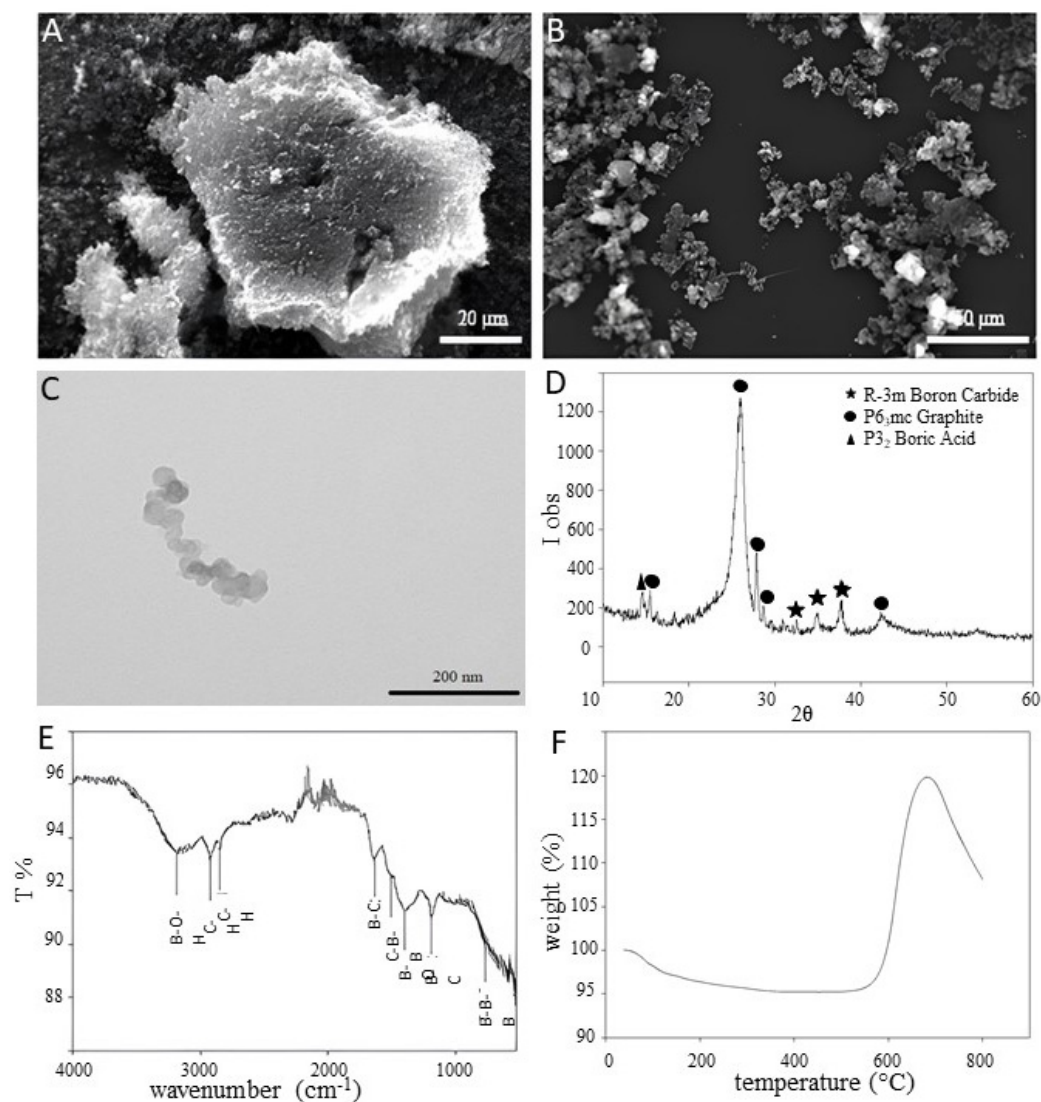


**Figure 1.** SEM images of pristine  $B_4C$  nanopowders (A) and  $B_4C$  NPs after treatment with an ultra-turrax (B): images were acquired at 15 kV with a SE; image B shows a significant decrease in agglomeration. TEM image of  $B_4C$  NPs following treatment with ultra-turrax, NPs appear irregularly shaped and polydispersed in size. (C) TEM images at lower magnifications could not provide useful information regarding an average size distribution due to the hydrophobic nature of pristine  $B_4C$ , which aggregates on the formvar coated grid. (D) XRD pattern of  $B_4C$  powders, showing R-3m diffraction peaks attributed to the rhombohedral structure of boron carbide. (E)  $\mu$ -FTIR spectra of  $B_4C$  NPs. (F)  $B_4C$  NPs' TGA curve in air.

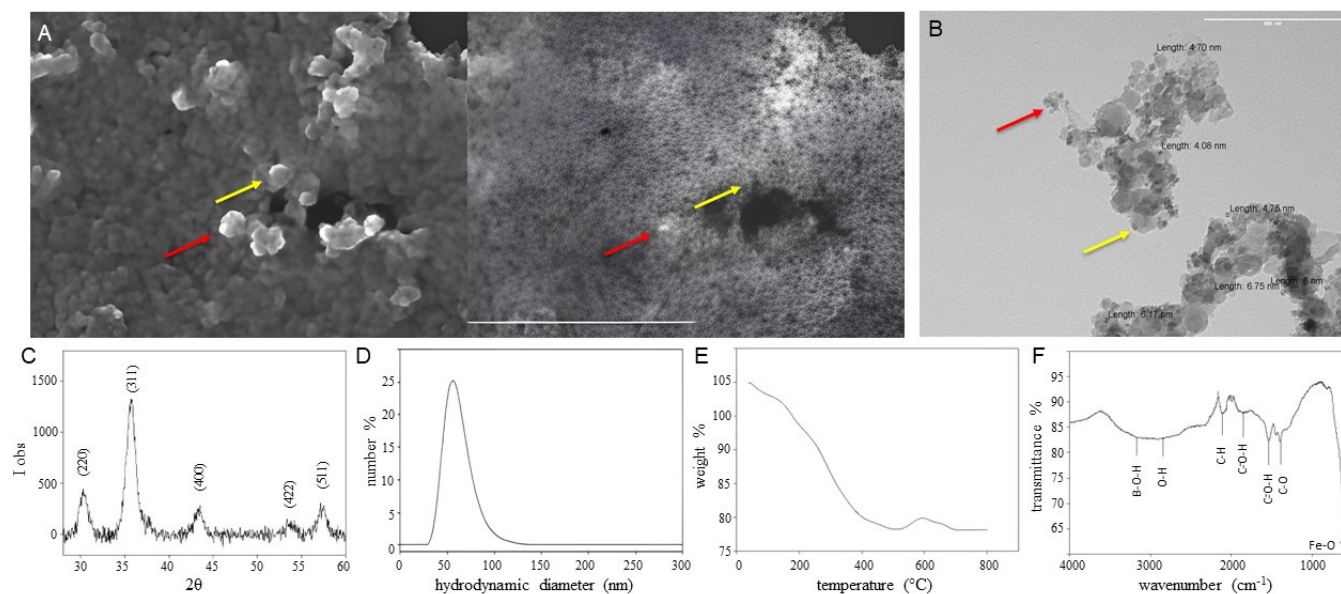


**Figure 2.** (A) SEM images of FeBNPs acquired with SE (left) and BSE (right) detectors show SPION (red arrows) distribution on B<sub>4</sub>C NPs (yellow arrows). Due to the low atomic weight of boron and carbon, EDS was not conducted to detect B<sub>4</sub>C NPs. (B) TEM images of FeBNPs diluted 1:500, both phases are visible and appear co-localized; however, SPIONs' distribution on B<sub>4</sub>C NPs appears irregular. (C) XRD pattern of FeBNPs; peaks corresponding to spinel structure attributable to Fe<sub>3</sub>O<sub>4</sub> NPs, with crystallite size 3.7(0.4) nm. (D) DLS analysis of FeBNPs; average hydrodynamic diameter 55(13) nm. (E) TGA curve of FeBNPs in air. (F) μ-FTIR spectra of FeBNPs confirm successful functionalization with PAA and the presence of SPIONs.

Figure 2E shows the TGA curve of produced FeBNPs when heated in air. The curve highlights three weight losses between 25 °C and 400 °C, which are ascribed to the dehydration of the sample, partial degradation of boric acid, decarboxylation of poly(acrylic acid) (155–225 °C) formation of anhydrides (225–300 °C), and their degradation (300–400 °C) [50]. At 600 °C, there is a 1.7 wt% increment in the sample weight due to oxidation, followed by a weight loss caused by the oxidation of carbon residues with the release of CO and CO<sub>2</sub>. The total mass loss is 22.1%.

The amount of total boron in FeBNPs was quantified through ICP. The concentration of total boron in the fraction of interest is 224 ppm; considering the natural abundance of <sup>10</sup>B in the starting B<sub>4</sub>C NPs powders (19.8% of total boron), the concentration of <sup>10</sup>B in FeBNPs is equal to 44.5 ppm.

### 3.3. FeBNPs' Interaction with HeLa Cells

FeBNPs' cytotoxicity was investigated through MTT assay. HeLa cells were incubated with FeBNPs diluted 1:10, 1:20, and 1:30 in the culture medium for 2 h and 6 h (Figure 3A). Cell viability is expressed as a percentage with respect to control cells (HeLa cells that had not undergone incubation with FeBNPs). No significant cytotoxicity was observed.

Scanning electron microscopy was performed on HeLa cells incubated with FeBNPs for different incubation times—30 min, 2 h, and 6 h—and different nanoparticles' dilutions in the media: 1:10 and 1:30. The adhesion of nanoparticles to the cell surface was observed after a 30 min incubation period (Figure 3B). Confocal microscopy evidenced the successful internalization of FeBNPs. Figure 3D illustrates that FeBNPs are predominantly internalized in proximity to the cells' nuclei. Confocal microscopy results agree with cytofluorimetric analysis (Figure 3C), establishing a correlation between an increased incubation time—as well as NP concentration in medium—and the heightened levels of both nanoparticle adhesion and internalization in HeLa cells.

The successful internalization was confirmed by TEM analysis. The images of Figure 4 evidence that the FeBNPs are probably internalized through a clathrin-mediated endocytosis and later accumulate in the cell's lysosomes and intracellular vesicles [51].

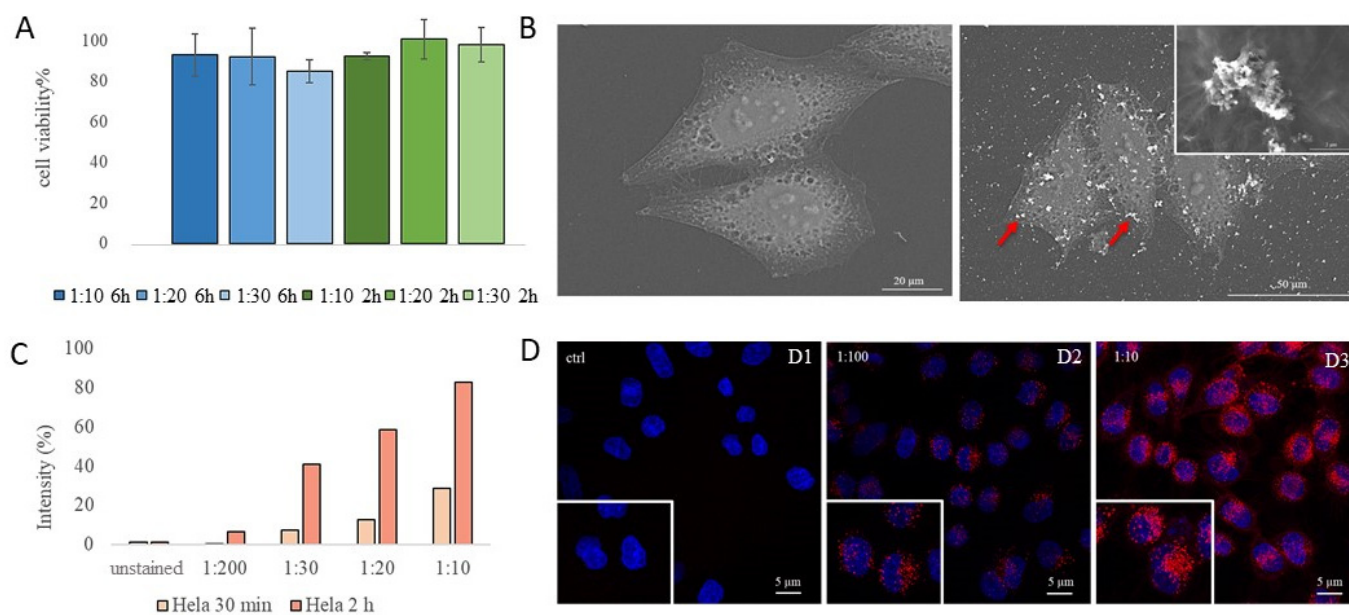


**Figure 3.** (A) MTT assay of HeLa cells incubated with FeBNPs diluted 1:10, 1:20, and 1:30 in the cell medium for 6 (blue) and 2 (green) hours. No significant cytotoxicity was observed. (B) Scanning electron microscopy pictures of HeLa cells' control sample (left) and HeLa cells incubated with FeBNPs (red arrows) diluted 1:30 in the medium for 30' (right). Nanoparticles' adhesion to HeLa cells can be appreciated even after short incubation times; magnification of FeBNPs adhering to the cells' membrane is provided in the top right-hand corner. (C) Cytofluorimetry results of HeLa cells incubated for 30 min and 2 h with different FeBNP concentrations; fluorescence intensity depends strongly on both nanoparticles' concentration and incubation time, increasing linearly with both increased incubation times and NP concentration. Representative experiment. (D) Confocal microscopy images of HeLa cells incubated with DiI-functionalized FeBNPs (FFeBNPs). (D1) Control sample (absence of FFeBNPs); HeLa cells incubated with FeBNPs 1:30 for 30 min (D2) and 2 h (D3).

The amount of  $^{10}\text{B}$  incorporated by the HeLa cells was quantified via optical inductively coupled plasma (ICP-OES). HeLa cells were incubated with FeBNPs diluted 1:30 in cell media ( $45\ \mu\text{g}$  of  $^{10}\text{B}/\text{mL}$ ). After 30 min of incubation, the  $^{10}\text{B}$  uptake was 25 ppm, corresponding to the therapeutic dose necessary for BNCT to succeed [2]. After 2 h of incubation with FeBNPs, the  $^{10}\text{B}$  uptake in HeLa cells had almost doubled to 49 ppm ( $\mu\text{g}\ ^{10}\text{B}/\text{g}$  of cells).

It must be noted that the microscopic analysis presented previously allows for the visualization of the distribution of FeBNPs within the cell population but does not show the actual distribution of the  $^{10}\text{B}$ . FeBNPs, in fact, are composite nanomaterials presenting part of the population containing iron oxide NPs alone. To evidence the distribution of  $^{10}\text{B}$  within the single cell and among different cells, intracellular neutron autoradiography was used. This technique allows us to simultaneously visualize the cells' localization and the tracks produced by the boron neutron capture on the same SSNTD [41,42,52,53]. The cells' imprints are created by exposing the SSNTD to UV-C radiation. This results in Fries photodegradation and photo-oxidation of the polymer in areas not protected by the cells. Staining the cells with hematoxylin before the UV-C irradiation allows for a higher resolution of the imprint and enhances the difference between the cells' nuclei and cytoplasm. Cells' nuclei, in fact, absorb more hematoxylin [54], which itself absorbs UV radiation, protecting the SSNTD from the photodegradation produced by the UV radiation.

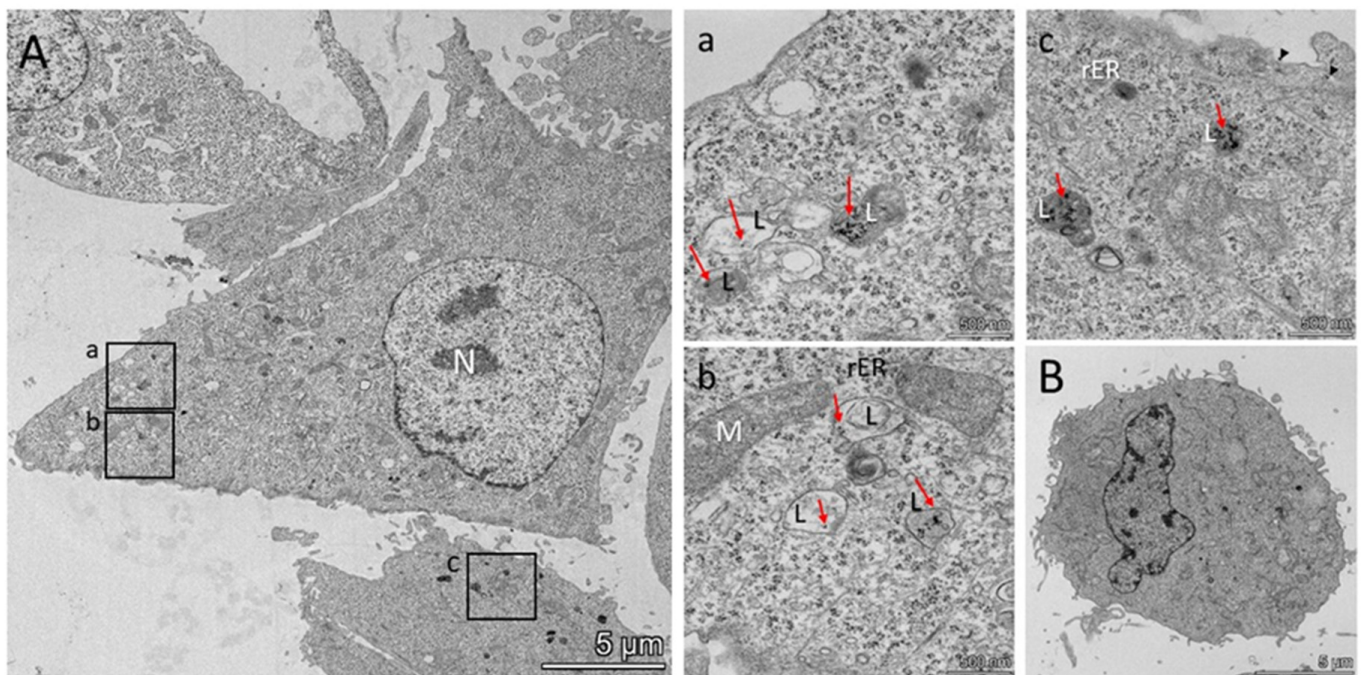


**Figure 4.** Transmission electron microscopy (TEM) images of HeLa cells following incubation with FeBNPs (red arrows). (A) A section of HeLa cells incubated with FeBNPs for 2 h is depicted. Subsections a, b, and c provide magnifications of the same image, elucidating the distinct presence of FeBNPs (red arrows) within the cells' lysosomes. (B) Control sample, HeLa cells—absence of FeBNPs. N: nuclei, L: lysosomes, M: mitochondria, rER: rough endoplasmic reticulum.

The development of the latent tracks that derive from the neutron capture reaction is carried out by chemical etching, which produces an enlargement of the track, rendering them visible by optical microscopy. It is critical to find the right timing for both etching and UV-C irradiation, in order to obtain the best resolution. An excessive UV-C irradiation, in fact, can lead to considerable track fading [43]. If properly performed, the technique allows for the visualization of the particle tracks as round pits of about 1  $\mu\text{m}$  in size, together with an image of the cell's distribution and internal structure. This characterization confirmed that FeBNPs are successfully internalized after just 30 min of incubation (Figure 5). In fact, after 30 min of incubation, about 60% of the cells presented internalized  $^{10}\text{B}$ , and after 2 h, 100% of the cells presented tracks either in the nuclear or in the cytoplasmic region when irradiated with a fluence of  $10^{13}$   $\text{n}/\text{cm}^2\text{s}$ . HeLa cells incubated with FeBNPs for 6 h were irradiated with  $10^{12}$  neutron fluence to limit the background noise on Lexan. In this case, it was impossible to carry out accurate  $^{10}\text{B}$  quantification due to the significant overlapping of the tracks deriving from the high local  $^{10}\text{B}$  density [43,52,53]. These results evidenced the presence of a relevant uptake of FeBNPs after 6 h of incubation that can lead to the delivery of high-LET secondary particles to the nuclei (Figure 5).

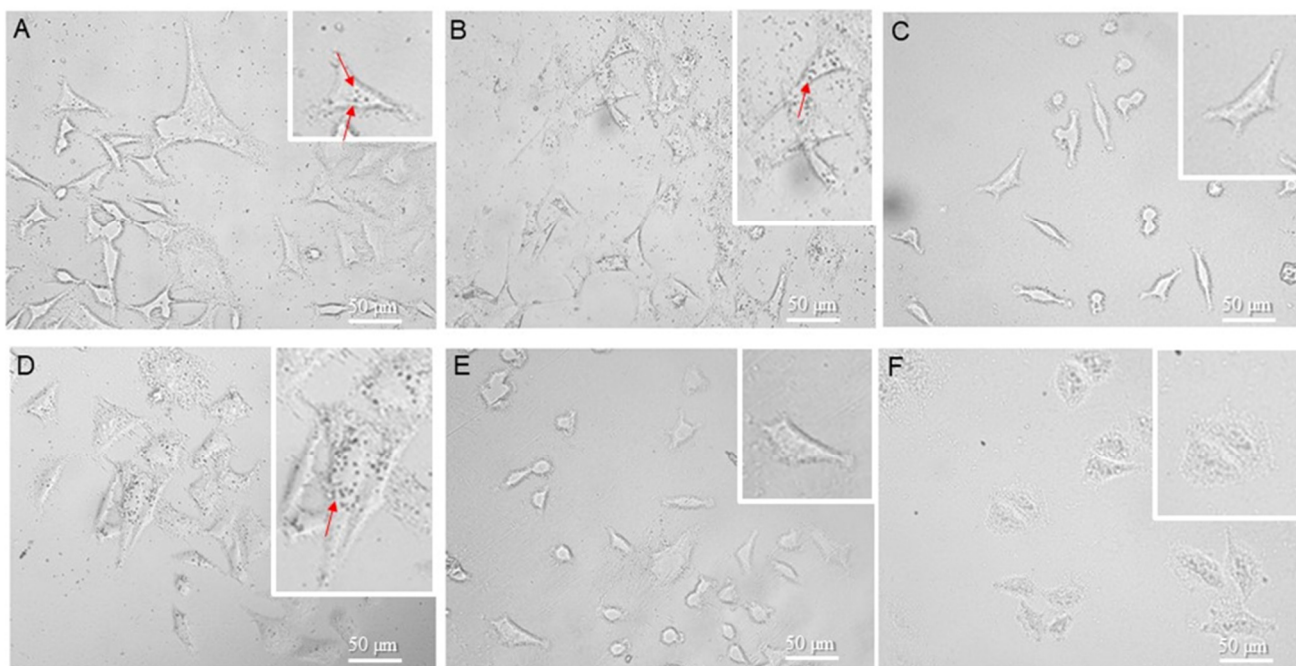


**Figure 5.** Optical microscopy pictures of HeLa cells' imprints on Lexan. Top: Samples irradiated  $10^{13}$  n/cm<sup>2</sup>s fluence; specifically imprints of HeLa cells incubated with FeBNPs (1:30) for 30 min (A), 2 h (B), and control sample (C). Tracks appear as round black dots, highlighted by red arrows. Bottom: Samples irradiated  $10^{12}$  n/cm<sup>2</sup>s fluence; specifically imprints of HeLa cells incubated with FeBNPs (1:30) for 6 h (D), control sample (E), control sample obtained without hematoxylin staining—which results in a worse imprint resolution (F). Top right corners: Magnifications of each picture; original magnification is  $40\times$ . It must be noted that cell imprints and tracks appear on two different focuses; pictures were acquired focusing on the tracks.

#### 4. Discussion

Boron neutron capture therapy provides a promising approach for the selective targeting of malignant cells while minimizing damage to surrounding healthy tissues. Effective BNCT hinges on the precise delivery of sufficient  $^{10}\text{B}$  to the tumor site, coupled with the administration of an adequate thermal neutron fluence ( $10^{12}$  cm<sup>-2</sup>) from an external radiation source. An ideal  $^{10}\text{B}$  carrier must achieve and maintain high concentrations within tumor tissues while presenting low systemic toxicity. The only boron isotope that contributes to BNCT is  $^{10}\text{B}$ , which presents a natural abundance of 19.8%. Hence, to reduce the pharmaceutical dose of boron agent in patients, a high level of enrichment is required. Furthermore, the effectiveness of BNCT, as a form of radiation therapy, relies not only on the concentration, but also on the precise localization of boron agents at the cellular level. While BSH (mercapto-undecahydro-*closo*-dodecaborate) was initially employed as the boron agent in BNCT for malignant brain tumors, its outcomes were deemed unsatisfactory, prompting its replacement by BPA (1,4-borono-L-phenylalanine), which is currently the most used boron agent in BNCT clinical trials [55]. However, because target tumor cells are unlikely to take up BPA homogeneously, there is a need to develop more efficient  $^{10}\text{B}$  carriers. In this context, inorganic boron compounds ( $\text{B}_4\text{C}$ , BN) represent promising candidates as they are chemically inert and present a high volumetric content of boron, possibly eliminating the need for enrichment.

In this work, we have developed a  $^{10}\text{B}$ -rich multifunctional nanomaterial derived from cost-effective, commercially available  $\text{B}_4\text{C}$ , including SPIONs and an optical fluorophore. The inclusion of  $\text{Fe}_3\text{O}_4$  NPs not only potentially allows for MRI imaging, but also for  $\text{B}_4\text{C}$  NP stabilization in aqueous media. These nanostructures exhibit remarkable stability in aqueous suspension, owing to the successful coating with poly (acrylic acid), and provide a substantial  $^{10}\text{B}$  concentration, eliminating the need for isotopic enrichment. It is important

to highlight that the boron carbide starting powders contained a notable proportion of impurities, likely comprising boron carbide precursors. Consequently, the actual boron carbide content in the powders represents approximately 30% of their total weight. Utilizing a pure B<sub>4</sub>C NP powder could potentially enable an even higher concentration of <sup>10</sup>B than that achieved thus far.

The presence of SPIONs and B<sub>4</sub>C NPs was confirmed in both aqueous suspension and biological environments. The functionalization with poly acrylic acid and DiI proved to be effective, resulting in the possibility to evidence the distribution of FeBNPs at the cellular level by confocal microscopy. FeBNPs are easily incorporated by HeLa cells, as demonstrated by several characterizations. However, the only technique able to localize <sup>10</sup>B at the cellular level and its distribution within the cells' population is intracellular neutron autoradiography. This analysis has demonstrated that FeBNPs present a tendency to accumulate near the cells' nuclei, suggesting a potential enhancement in therapeutic efficacy. It is crucial to consider this aspect while developing <sup>10</sup>B carriers for BNCT, as the ultimate cause of cell death after exposure to a lethal dose of ionizing radiation is DNA damage. In fact, cells typically possess the ability to repair DNA lesions, unless they present extensive genome damage. As the secondary particles produced by the neutron capture ( $\alpha$ , <sup>7</sup>Li<sup>3+</sup>) present high linear energy transfer characteristics, they deposit large amounts of energy within a short free path length [56]. This represents concurrently the advantage of BNCT, that is, its high selectivity, and a challenge while developing new boron agents. For the produced nanomaterials, the <sup>10</sup>B uptake resulted to be double the therapeutic dose reported in the literature for BNCT, after just 2 h of incubation. These observations represent a promising result considering the possible use of nanomaterials in BCNT treatment. Future investigations will delve into the evaluation of the magnetic properties of FeBNPs, and the persistence of these nanomaterials in biological systems. Their effectiveness in vivo will also be investigated through an assessment of cell survival and damage.

## 5. Conclusions

BNCT provides a safe way to deliver high-LET ionizing radiation to cancerous cells, inducing complex lesions in the DNA that are difficult to repair. A significant current challenge in this field is the lack of specific boron carriers capable of selectively targeting tumor cells. Our research has led to the development of <sup>10</sup>B-rich stable nanomaterials that can deliver large amounts of high-LET particles in the nuclear region of the HeLa cell line used in this work. These nanomaterials might avoid the use of isotopically enriched compounds and, due to their inert chemical nature, might exhibit prolonged retention at tumor sites, thereby enabling high tumor-to-normal tissue ratios. Further investigations are required to precisely target tumor sites and explore the potential applications of these composite nanomaterials in MRI.

**Author Contributions:** Conceptualization, M.P.D., U.A.-T. and P.S.; methodology, M.P.D., A.V., V.F., P.S., A.M.P., M.A.G., A.F., E.V. and I.P.; data analysis, M.P.D., A.M.P., A.V., P.S., A.F. and E.V.; investigation, M.P.D., A.M.P. and P.S.; resources, U.A.-T., P.S., S.B. and A.M.P.; data curation, M.P.D. and P.S.; manuscript preparation, M.P.D.; review and editing, M.P.D., U.A.-T., P.S., A.M.P., S.B. and C.M. All authors have read and agreed to the published version of the manuscript.

**Funding:** The work was partially funded by INFN, grant ENTER\_BNCT of CSN5. Measurements by neutron autoradiography were performed in the frame of the CUIA-CONICET 2022 project 'Distribution and intracellular concentration of borated compounds for the study of dose-effect in neutron radiotherapy'.

**Institutional Review Board Statement:** Not applicable.

**Informed Consent Statement:** Not applicable.

**Data Availability Statement:** The raw data supporting the conclusions of this article will be made available by the authors on request.

**Acknowledgments:** We are grateful to Centro Interdipartimentale di Studi e Ricerca per la Conservazione del Patrimonio Culturale (CISRIc), University of Pavia, for providing access to HRSEM and Centro Grandi Strumenti (CGS), University of Pavia, for confocal microscopy, specifically to Amanda Oldani (CGS). We are also grateful to Federica Maraschi and Antonella Profumo for carrying out ICP measurements, and to the RA-3 team for irradiating the neutron autoradiographic samples at the thermal neutron column and to the researchers at the Laboratory of Nuclear Tracks and Neutron Autoradiography of CNEA for their collaboration with the autoradiography experiments.

**Conflicts of Interest:** The authors declare no conflicts of interest. The funders had no role in the design of the study; in the collection, analyses, or interpretation of data; in the writing of the manuscript; or in the decision to publish the results.

## References

1. Jin, W.H.; Seldon, C.; Butkus, M.; Sauerwein, W.; Giap, H.B. A Review of Boron Neutron Capture Therapy: Its History and Current Challenges. *Int. J. Part. Ther.* **2022**, *9*, 71–82. [CrossRef]
2. Barth, R.F.; Mi, P.; Yang, W. Boron Delivery Agents for Neutron Capture Therapy of Cancer. *Cancer Commun.* **2018**, *38*, 35. [CrossRef]
3. Monti Hughes, A.; Hu, N. Optimizing Boron Neutron Capture Therapy (BNCT) to Treat Cancer: An Updated Review on the Latest Developments on Boron Compounds and Strategies. *Cancers* **2023**, *15*, 4091. [CrossRef]
4. Dymova, M.A.; Taskaev, S.Y.; Richter, V.A.; Kuligina, E.V. Boron Neutron Capture Therapy: Current Status and Future Perspectives. *Cancer Commun.* **2020**, *40*, 406–421. [CrossRef]
5. Xuan, S.; Vicente, M.G.H. *Recent Advances in Boron Delivery Agents for Boron Neutron Capture Therapy (BNCT)*; Wiley Online Library: Hoboken, NJ, USA, 2018. [CrossRef]
6. Zhang, Z.; Chong, Y.; Liu, Y.; Pan, J.; Huang, C.; Sun, Q.; Liu, Z.; Zhu, X.; Shao, Y.; Jin, C.; et al. A Review of Planned, Ongoing Clinical Studies and Recent Development of BNCT in Mainland of China. *Cancers* **2023**, *15*, 4060. [CrossRef]
7. Moss, R.L. Critical Review, with an Optimistic Outlook, on Boron Neutron Capture Therapy (BNCT). *Appl. Radiat. Isot.* **2014**, *88*, 2–11. [CrossRef]
8. Malouff, T.D.; Seneviratne, D.S.; Ebner, D.K.; Stross, W.C.; Waddle, M.R.; Trifiletti, D.M.; Krishnan, S. Boron Neutron Capture Therapy: A Review of Clinical Applications. *Front. Oncol.* **2021**, *11*, 601820. [CrossRef]
9. Suzuki, M.; Kato, I.; Aihara, T.; Hiratsuka, J.; Yoshimura, K.; Niimi, M.; Kimura, Y.; Ariyoshi, Y.; Haginomori, S.I.; Sakurai, Y.; et al. Boron Neutron Capture Therapy Outcomes for Advanced or Recurrent Head and Neck Cancer. *J. Radiat. Res.* **2014**, *55*, 146–153. [CrossRef]
10. Tsuji, T.; Yoshitomi, H.; Ishikawa, Y.; Koshizaki, N.; Suzuki, M.; Usukura, J. A Method to Selectively Internalise Submicrometer Boron Carbide Particles into Cancer Cells Using Surface Transferrin Conjugation for Developing a New Boron Neutron Capture Therapy Agent. *J. Exp. Nanosci.* **2020**, *15*, 1–11. [CrossRef]
11. Takai, S.; Wanibuchi, M.; Kawabata, S.; Takeuchi, K.; Sakurai, Y.; Suzuki, M.; Ono, K.; Miyatake, S.I. Reactor-Based Boron Neutron Capture Therapy for 44 Cases of Recurrent and Refractory High-Grade Meningiomas with Long-Term Follow-Up. *Neuro-Oncol.* **2022**, *24*, 90–98. [CrossRef]
12. Blue, T.E.; Yanch, J.C. Accelerator-based epithermal neutron sources for Boron Neutron Capture Therapy of brain tumors. *J. Neuro-Oncol.* **2003**, *62*, 19–31. [CrossRef]
13. Oloo, S.O.; Smith, K.M.; Vicente, M.D.G.H. Multi-Functional Boron-Delivery Agents for Boron Neutron Capture Therapy of Cancers. *Cancers* **2023**, *15*, 3277. [CrossRef] [PubMed]
14. Capoulat, M.E.; Kreiner, A.J. Induced radioactivity in AB-BNCT: An analysis of the different facilities worldwide. *Front. Nucl. Eng.* **2023**, *2*, 1275396. [CrossRef]
15. Cartelli, D.E.; Capoulat, M.E.; Baldo, M.; Sandin Suarez, J.C.; Igarzabal, M.; del Grosso, M.F.; Valda, A.A.; Canepa, N.; Minsky, D.M.; Conti, G.; et al. Status of low-energy accelerator-based BNCT worldwide and in Argentina. *Appl. Radiat. Isot.* **2020**, *166*, 109315. [CrossRef]
16. Bortolussi, S.; Postuma, I.; Protti, N.; Provenzano, L.; Ferrari, C.; Cansolino, L.; Dionigi, P.; Galasso, O.; Gasparini, G.; Altieri, S.; et al. Understanding the Potentiality of Accelerator Based-Boron Neutron Capture Therapy for Osteosarcoma: Dosimetry Assessment Based on the Reported Clinical Experience. *Radiat. Oncol.* **2017**, *12*, 130. [CrossRef]
17. Kreiner, A.J.; Bergueiro, J.; Cartelli, D.; Baldo, M.; Castell, W.; Asoia, J.G.; Padulo, J.; Suárez Sandín, J.C.; Igarzabal, M.; Erhardt, J.; et al. Present Status of Accelerator-Based BNCT. *Rep. Pract. Oncol. Radiother.* **2016**, *21*, 95–101. [CrossRef]
18. Yinghuai, Z.; Cheng Yan, K.; Maguire, J.A.; Hosmane, N.S. Recent Developments in Boron Neutron Capture Therapy (BNCT) Driven by Nanotechnology. *Curr. Chem. Biol.* **2008**, *1*, 141–149. [CrossRef]
19. Beck-Sickinger, A.G.; Becker, D.P.; Chepurna, O.; Das, B.; Flieger, S.; Hey-Hawkins, E.; Hosomanie, N.; Jalisatgi, S.S.; Nakamura, H.; Patil, R.; et al. New Boron Delivery Agents. *Cancer Biother. Radiopharm.* **2023**, *38*, 160–172. Available online: <https://pubmed.ncbi.nlm.nih.gov/36350709/> (accessed on 18 March 2024). [CrossRef] [PubMed]
20. Zhang, X.; Lin, Y.; Hosmane, N.S.; Zhu, Y. Nanostructured Boron Agents for Boron Neutron Capture Therapy: A Review of Recent Patents. *Med. Rev.* **2023**, *3*, 425–443. [CrossRef]

21. Singh, B.; Kaur, G.; Singh, P.; Singh, K.; Kumar, B.; Vij, A.; Kumar, M.; Bala, R.; Meena, R.; Singh, A.; et al. Nanostructured Boron Nitride with High Water Dispersibility for Boron Neutron Capture Therapy. *Sci. Rep.* **2016**, *6*, 35535. [[CrossRef](#)]
22. Paul, W.; Sharma, C.P. *Inorganic Nanoparticles for Targeted Drug Delivery*; Elsevier Ltd.: Amsterdam, The Netherlands, 2019. [[CrossRef](#)]
23. Gosset, D. Basic Properties of Boron Carbide. *Compr. Nucl. Mater. (Second Ed.)* **2020**, *7*, 539–553. [[CrossRef](#)]
24. Tatiya, S.; Pandey, M.; Bhattacharya, S. Nanoparticles Containing Boron and Its Compounds—Synthesis and Applications: A Review. *J. Micromanufacturing* **2020**, *3*, 159–173. [[CrossRef](#)]
25. Yoshie Ishikawa, T.I. Boron Carbide Particle as a Boron Compound for Boron Neutron Capture Therapy. *J. Nucl. Med. Radiat. Ther.* **2014**, *5*, 2–6. [[CrossRef](#)]
26. Mortensen, M.W.; Sørensen, P.G.; Björkdahl, O.; Jensen, M.R.; Gundersen, H.J.G.; Bjørnholm, T. Preparation and Characterization of Boron Carbide Nanoparticles for Use as a Novel Agent in T Cell-Guided Boron Neutron Capture Therapy. *Appl. Radiat. Isot.* **2006**, *64*, 315–324. [[CrossRef](#)]
27. Mortensen, M.W.; Björkdahl, O.; Sørensen, P.G.; Hansen, T.; Jensen, M.R.; Gundersen, H.J.G.; Bjørnholm, T. Functionalization and Cellular Uptake of Boron Carbide Nanoparticles. The First Step toward T Cell-Guided Boron Neutron Capture Therapy. *Bioconj. Chem.* **2006**, *17*, 284–290. [[CrossRef](#)]
28. Vitali, A.; Demichelis, M.P.; Di Martino, G.; Postuma, I.; Bortolussi, S.; Falqui, A.; Milanese, C.; Ferrara, C.; Sommi, P.; Anselmi-Tamburini, U. Synthesis and Characterization of Gd-Functionalized B<sub>4</sub>C Nanoparticles for BNCT Applications. *Life* **2023**, *13*, 429. [[CrossRef](#)]
29. Kozień, D.; Żeliszewska, P.; Szermer-Olearnik, B.; Adamczyk, Z.; Wróblewska, A.; Szczygieł, A.; Węgierek-Ciura, K.; Mierzejewska, J.; Pajtasz-Piasecka, E.; Tokarski, T.; et al. Synthesis and Characterization of Boron Carbide Nanoparticles as Potential Boron-Rich Therapeutic Carriers. *Materials* **2023**, *16*, 6534. [[CrossRef](#)] [[PubMed](#)]
30. Wallyn, J.; Anton, N.; Vandamme, T.F. Synthesis, Principles, and Properties of Magnetite Nanoparticles for in Vivo Imaging Applications—A Review. *Pharmaceutics* **2019**, *11*, 601. [[CrossRef](#)] [[PubMed](#)]
31. Jeon, M.; Halbert, M.V.; Stephen, Z.R.; Zhang, M. Iron Oxide Nanoparticles as T1 Contrast Agents for Magnetic Resonance Imaging: Fundamentals, Challenges, Applications, and Prospectives. *Adv. Mater.* **2021**, *33*, 1906539. [[CrossRef](#)] [[PubMed](#)]
32. Stephen, Z.R.; Kievit, F.M.; Zhang, M. Magnetite Nanoparticles for Medical MR Imaging. *Mater. Today* **2011**, *14*, 330–338. [[CrossRef](#)]
33. Thakor, A.S.; Jokerst, J.V.; Ghanouni, P.; Campbell, J.L.; Mittra, E.; Gambhir, S.S. Clinically Approved Nanoparticle Imaging Agents. *J. Nucl. Med.* **2016**, *57*, 1833–1837. [[CrossRef](#)]
34. Revia, R.A.; Zhang, M. Magnetite Nanoparticles for Cancer Diagnosis, Treatment, and Treatment Monitoring: Recent Advances. *Mater. Today* **2016**, *19*, 157–168. [[CrossRef](#)]
35. Aladesuyi, O.A.; Oluwafemi, S.O. The role of magnetic nanoparticles in cancer management. *Nano-Struct. Nano-Objects* **2023**, *36*, 101053. [[CrossRef](#)]
36. Chengyin, F.; Ravindra, N.M. Magnetic iron oxide nanoparticles: Synthesis and applications. *Bioinspired Biomim. Nanobiomaterials* **2012**, *1*, 229–244. [[CrossRef](#)]
37. Santra, S.; Kaittanis, C.; Grimm, J.; Perez, J.M. Drug/Dye-Loaded, Multifunctional Iron Oxide Nanoparticles for Combined Targeted Cancer Therapy and Dual Optical/Magnetic Resonance Imaging. *Small* **2009**, *5*, 1862–1868. [[CrossRef](#)] [[PubMed](#)]
38. Stockert, J.C.; Horobin, R.W.; Colombo, L.L.; Blázquez-Castro, A. Tetrazolium Salts and Formazan Products in Cell Biology: Viability Assessment, Fluorescence Imaging, and Labeling Perspectives. *Acta Histochem.* **2018**, *120*, 159–167. [[CrossRef](#)]
39. Tan, X.; Zhou, R.; Feng, Y.; Liang, T. In-Depth Method Investigation for Determination of Boron in Silicate Samples Using an Improved Boron–Mannitol Complex Digestion Method by Inductively Coupled Plasma Mass Spectrometry. *Molecules* **2023**, *28*, 441. [[CrossRef](#)] [[PubMed](#)]
40. Sah, R.N.; Brown, P.H. Boron Determination—A Review of Analytical Methods. *Microchem. J.* **1997**, *304*, 285–304. [[CrossRef](#)]
41. Portu, A.; Rossini, A.E.; Thorp, S.I.; Curotto, P.; Pozzi, E.C.C.; Granell, P.; Golmar, F.; Cabrini, R.L.; Martin, G.S. Simultaneous Observation of Cells and Nuclear Tracks from the Boron Neutron Capture Reaction by UV-C Sensitization of Polycarbonate. *Microsc. Microanal.* **2015**, *21*, 796–804. [[CrossRef](#)] [[PubMed](#)]
42. Gadan, M.A.; Lloyd, R.; Saint Martin, G.; Olivera, M.S.; Policastro, L.; Portu, A.M. Neutron Autoradiography Combined with UV-C Sensitization: Toward the Intracellular Localization of Boron. *Microsc. Microanal.* **2019**, *25*, 1331–1340. [[CrossRef](#)] [[PubMed](#)]
43. Portu, A.M.; Spain, M.S.; Thorp, S.I.; Trivillin, V.A.; Curotto, P.; Monti Hughes, A.; Pozzi, E.C.C.; Garabalino, M.A.; Palmieri, M.A.; Granell, P.N.; et al. Enhanced Resolution of Neutron Autoradiography with UV-C Sensitization to Study Boron Microdistribution in Animal Models. *Life* **2023**, *13*, 1578. [[CrossRef](#)] [[PubMed](#)]
44. Sezer, A.O.; Brand, J.I. Chemical Vapor Deposition of Boron Carbide. *Mater. Sci. Eng.* **2019**, *79*, 191–202. [[CrossRef](#)]
45. Suri, A.K.; Subramanian, C.; Sonber, J.K.; Ch Murthy, T.S.R. Synthesis and Consolidation of Boron Carbide: A Review. *Int. Mater. Rev.* **2010**, *55*, 4–40. [[CrossRef](#)]
46. Kiliçarslan, A.; Toptan, F.; Kerti, I.; Piskin, S. Oxidation of Boron Carbide Particles at Low Temperatures. *Mater. Lett.* **2014**, *128*, 224–226. [[CrossRef](#)]
47. Kozień, D.; Jelén, P.; Stepién, J.; Olejniczak, Z.; Sitarz, M.; Pedzich, Z. Surface Properties and Morphology of Boron Carbide Nanopowders Obtained by Lyophilization of Saccharide Precursors. *Materials* **2021**, *14*, 3419. [[CrossRef](#)]

48. Rotaru, A. Thermal and Kinetic Study of Hexagonal Boric Acid versus Triclinic Boric Acid in Air Flow. *J. Therm. Anal. Calorim.* **2017**, *127*, 755–763. [[CrossRef](#)]
49. Jain, A.; Anthonyasamy, S. Oxidation of Boron Carbide powder. *J. Therm. Anal. Calorim.* **2015**, *122*, 645–652. [[CrossRef](#)]
50. Bin-Dahman, O.A.; Jose, J.; Al-Harhi, M.A. Compatibility of Poly(Acrylic Acid)/Starch Blends. *Starch/Staerke* **2015**, *67*, 1061–1069. [[CrossRef](#)]
51. Sousa de Almeida, M.; Susnik, E.; Drasler, B.; Taladriz-Blanco, P.; Petri-Fink, A.; Rothen-Rutishauser, B. Understanding nanoparticle endocytosis to improve targeting strategies in nanomedicine. *Chem. Soc. Rev.* **2021**, *50*, 5397. [[CrossRef](#)]
52. Saint Martin, G.; Portu, A.M.; Ibarra, M.L.; Alurralde, M. UV-C Radiation Effect on Nuclear Tracks of Different Ions in Polycarbonate. *Radiat. Phys. Chem.* **2020**, *173*, 108936. [[CrossRef](#)]
53. Portu, A.; Postuma, I.; Gadan, M.A.; Saint Martin, G.; Olivera, M.S.; Altieri, S.; Protti, N.; Bortolussi, S. Reprint of Inter-Comparison of Boron Concentration Measurements at INFN-University of Pavia (Italy) and CNEA (Argentina). *Appl. Radiat. Isot.* **2015**, *106*, 171–175. [[CrossRef](#)] [[PubMed](#)]
54. Langenbacher, R.E.; Horoszko, C.P.; Kim, M.; Heller, D. Hematoxylin Nuclear Stain Reports Oxidative Stress via Near-Infrared Emission. *ACS Chem. Biol.* **2023**, *18*, 1237–1245. [[CrossRef](#)] [[PubMed](#)]
55. International Atomic Energy Agency. *Advances in Boron Neutron Capture Therapy*; IAEAAL 23-01601 (paperback: Alk. paper); International Atomic Energy Agency: Vienna, Austria, 2023; ISBN 978-92-0-132723-9/978-92-0-132623-2.
56. Mechetin, G.V.; Zharkov, D.O. DNA Damage Response and Repair in Boron Neutron Capture Therapy. *Genes* **2023**, *14*, 127. [[CrossRef](#)] [[PubMed](#)]

**Disclaimer/Publisher's Note:** The statements, opinions and data contained in all publications are solely those of the individual author(s) and contributor(s) and not of MDPI and/or the editor(s). MDPI and/or the editor(s) disclaim responsibility for any injury to people or property resulting from any ideas, methods, instructions or products referred to in the content.